

The Reservoir of the Per-emb-2 Streamer

KOTOMI TANIGUCHI,¹ JAIME E PINEDA,² PAOLA CASELLI,² TOMOMI SHIMOIKURA,³ RACHEL K. FRIESEN,⁴
 DOMINIQUE M. SEGURA-COX,^{5,2,*} AND ANIKA SCHMIEDEKE⁶

¹National Astronomical Observatory of Japan, National Institutes of Natural Sciences, 2-21-1 Osawa, Mitaka, Tokyo 181-8588, Japan

²Center for Astrochemical Studies, Max-Planck-Institut für Extraterrestrische Physik, Gießenbachstrasse 1, D-85741 Garching bei München, Germany

³Faculty of Social Information Studies, Otsuka Women's University, Sanban-cho, Chiyoda, Tokyo 102-8357, Japan

⁴Department of Astronomy & Astrophysics, University of Toronto, 50 St. George St., Toronto, ON, M5S 3H4, Canada

⁵Department of Astronomy, The University of Texas at Austin, 2500 Speedway, Austin, TX 78712, USA

⁶Green Bank Observatory, PO Box 2, Green Bank, WV 24944, USA

ABSTRACT

Streamers bring gas from outer regions to protostellar systems and could change the chemical composition around protostars and protoplanetary disks. We have carried out mapping observations of carbon-chain species (HC_3N , HC_5N , CCH, and CCS) in the 3mm and 7mm bands toward the streamer flowing to the Class 0 young stellar object (YSO) Per-emb-2 with the Nobeyama 45m radio telescope. A region with a diameter of ~ 0.04 pc is located north with a distance of $\sim 20,500$ au from the YSO. The streamer connects to this north region which is the origin of the streamer. The reservoir has high density and low temperature ($n_{\text{H}_2} \approx 1.9 \times 10^4 \text{ cm}^{-3}$, $T_{\text{kin}} = 10 \text{ K}$), which are similar to those of early stage starless cores. By comparisons with the observed abundance ratios of CCS/ HC_3N to the chemical simulations, the reservoir and streamer are found to be chemically young. The total mass available for the streamer is derived to be $24 - 34 \text{ M}_{\odot}$. If all of the gas in the reservoir will accrete onto the Per-emb-2 protostellar system, the lifetime of the streamer has been estimated at $(1.1 - 3.2) \times 10^5$ yr, suggesting that the mass accretion via the streamer would continue until the end of the Class I stage.

Keywords: Astrochemistry (75) — Low mass stars (2050) — Star formation (1569) — Young stellar objects (1834)

1. INTRODUCTION

Streamers, velocity coherent structures funneling material around young stellar objects (YSOs), bring gas from outer regions to the disk forming regions (for a review see Pineda et al. 2023). The outer gas would have different chemical compositions from the gas close to YSOs and then these streamers could change the chemical composition at the protoplanetary disks and/or the protostellar cores. Their kinematic structures are composed of a smooth velocity gradient driven by gravity and rotation. Streamers may play essential roles during the formation of the solar system (Arzoumanian et al.

2023). Thus, it is important to reveal the physics and chemistry of these streamer structures to understand the star and planet formation including our solar system.

Many observations with interferometers have revealed the presence of streamers toward various evolutionary stage YSOs; highly embedded Class 0 phase (Le Gouellec et al. 2019; Pineda et al. 2020), Class I stage (Chou et al. 2016; Valdivia-Mena et al. 2022), and Class II stage (Ginski et al. 2021; Garufi et al. 2022). Similar infall gas structures feeding circumbinary disks around binary systems have also been found (Takakuwa et al. 2017; Alves et al. 2019). In addition, triple spiral arms connected to a triple protostellar system IRAS 042329+2436 have been found using the SO emission as seen by the Atacama Large Millimeter/submillimeter Array (ALMA, Lee et al. 2023). They compared the observational results with numerical simulations and suggested that the large triple spiral arms are produced by gravitational

Corresponding author: Kotomi Taniguchi
 kotomi.taniguchi@nao.ac.jp

* NSF Astronomy and Astrophysics Postdoctoral Fellow

interactions between compact triple protostars and the turbulent infalling envelope. In the high-mass regime, Schwörer et al. (2019) found converging flows toward the high-mass star-forming cluster Sagittarius B2 (N). The protostellar system GGD 27-MM1 has been shown to present streamers (Fernández-López et al. 2023). Thus, mass accretion via streamers seems to occur in various protostellar systems.

These streamers are traced by several molecular lines: carbon-chain species (e.g., HC₃N (Pineda et al. 2020) and HC₅N (Murillo et al. 2022)), DCN (Hsieh et al. 2023), CS, HCO⁺ (Garufi et al. 2022), H₂CO, SO and SO₂ (Valdivia-Mena et al. 2022). Some of the tracers are likely common among protostellar systems, but others may be unique for each source. The chemical composition differs between streamers, and suitable tracers would be related to the origin of the streamer and/or environment.

Many numerical simulations could explain the origin of the streamers (for a review see Pineda et al. 2023). Seifried et al. (2015) showed that the accretion in the vicinity of protostellar disks is highly anisotropic in their simulations including turbulence and magnetic fields. Gas capture, where sweeping up gas via Bondi-Hoyle accretion occurs, causes the formation of filamentary arms which appear as accretion streamers (Bate 2018). Another possibility is interactions of a star-disk system with an external perturber such as binary components or a stellar fly-by (e.g., Vorobyov et al. 2017; Cuello et al. 2020). We need large-scale mapping observations of the protostellar systems covering their streamers to reveal the mechanisms of the streamers.

The Class 0 YSO IRAS 03292+3039, also known as Per-emb-2, is a protostellar system located in the Perseus star-forming region ($d = 300$ pc; Zucker et al. 2018). No complex organic molecules (COMs) except for CH₃OH were detected in the Perseus ALMA Chemistry Survey (PEACHES; Yang et al. 2021), and this source is likely a chemically-poor source. Outflows have been detected with CO lines along the northwest (red shifted) - southeast (blue shifted) direction (Stephens et al. 2019).

Pineda et al. (2020) discovered a streamer of this protostellar system with observations using the NOrthern Extended Millimeter Array (NOEMA). The streamer structure can be seen well in the emission lines of carbon-chain species, such as HC₃N and CCS. On the other hand, the emission of N₂H⁺ and its deuterated isotopologue N₂D⁺ is not consistent with the streamer structure. This suggests that chemically fresh gas is brought to the disk scale via the streamer (Suzuki et al. 1992; Benson et al. 1998). Pineda et al. (2020) estimated the

mass of the streamer and its infall rate at $0.1 M_{\odot}$ and $10^{-6} M_{\odot} \text{ yr}^{-1}$, respectively, although with a poorly constrained abundance. The starting point of the streamer and its total mass budget remain unrevealed.

In this paper, we present mapping observations of four carbon-chain molecules, HC₃N, HC₅N, CCH, and CCS, in the 3mm and 7mm bands toward the streamer of the YSO Per-emb-2 with the Nobeyama 45m radio telescope. We describe the observations and data reduction in Section 2.1. We present analyses including available data obtained by the IRAM 30m telescope and 100m Green Bank Telescope (GBT). We briefly describe these observations in Sections 2.2 and 2.3, respectively. Maps obtained by the Nobeyama 45m telescope and line analyses are presented in Sections 3.1 and 3.2, respectively. We compare the observed CCS/HC₃N abundance ratios to the chemical models to constrain the HC₃N abundances (Section 4.1) and derive the total mass of the streamer (Section 4.2). We calculate the streamer infall rate and the lifetime of the streamer in Section 4.3. Our main conclusions are summarized in Section 5.

2. OBSERVATIONS AND DATA REDUCTION

2.1. Nobeyama 45m radio telescope

We carried out observations with the Nobeyama 45m radio telescope in November and December 2022 and from February to April 2023 (Proposal Number: G22006, PI: Kotomi Taniguchi). FOREST (FOur beam REceiver System on the 45m Telescope; Minamidani et al. 2016) and Z45 (Nakamura et al. 2015) receivers were used for the 3mm and 7mm observations, respectively. The beam size and main beam efficiency (η_{MB}) of FOREST are 18'' and 50%, and those of Z45 are 37'' and 70%, respectively. System temperatures (T_{sys}) were $\sim 170 - 300$ K at the 3mm band and $\sim 120 - 200$ K at the 7mm band, depending on the weather condition and elevation. The chopper-wheel method was applied for the calibration, and typical calibration errors were 10% (Taniguchi et al. 2017).

Target lines in each frequency band are summarized in Table 1. As our target streamer is expected to have chemically young features as mentioned in Section 1, we selected carbon-chain species which are known to be abundant in young starless cores (Suzuki et al. 1992; Benson et al. 1998). In addition, SiO and HNCO, both of which are shock tracers (e.g., Rodríguez-Fernández et al. 2010; Podio et al. 2017), were observed simultaneously in the 7mm band.

We used the SAM45 FX-type digital correlator (Kamazaki et al. 2012). The frequency resolutions were

Table 1. Information on the targeted lines

| Species | Transition | E_{up}/k (K) | Frequency (GHz) |
|---|---|--------------------------|--------------------|
| Nobeyama 3mm band observations | | | |
| HC ₃ N | $J = 9 - 8$ | 19.6 | 81.8814677 |
| CCS | $J_N = 7_6 - 6_5$ | 15.4 | 81.5051700 |
| CCS | $J_N = 6_7 - 5_6$ | 23.3 | 86.1813910 |
| CCH | $N = 1 - 0, J = \frac{3}{2} - \frac{1}{2}, F = 2 - 1$ | 4.2 | 87.3169250 |
| Nobeyama 7mm band observations | | | |
| HC ₃ N | $J = 5 - 4$ | 6.5 | 45.4903138 |
| HC ₅ N | $J = 16 - 15$ | 17.4 | 42.6021529 |
| HC ₅ N | $J = 17 - 16$ | 19.6 | 45.2647199 |
| CCS | $J_N = 4_3 - 3_2$ | 5.4 | 45.3790460 |
| CC ³⁴ S | $J_N = 4_3 - 3_2$ | 5.3 | 44.4975990 |
| cyclic-C ₃ H ₂ | $J_{Ka,Kc} = 3_{2,1} - 3_{1,2}$ | 18.2 | 44.1047769 |
| SiO | $J = 1 - 0$ | 2.1 | 43.4237600 |
| HNCO | $2_{0,2} - 1_{0,1}, F = 2 - 1$ | 3.2 | 43.9630395 |
| IRAM 30m telescope observations | | | |
| HC ₃ N | $J = 8 - 7$ | 15.7 | 72.783822 |
| HC ₃ N | $J = 10 - 9$ | 24.0 | 90.979023 |
| Green Bank 100m telescope observations | | | |
| CCS | $J_N = 2_1 - 1_2$ | 1.6 | 22.3440308 |

NOTE—Rest frequencies are taken from the Cologne Database for Molecular Spectroscopy (CDMS; Müller et al. 2005; Endres et al. 2016), except for CC³⁴S which is taken from the JPL catalog (Pickett et al. 1998). We summarize only utilized lines in this paper for observations with the IRAM 30m and Green Bank 100m telescopes.

30.52 kHz and 15.26 kHz for the 3mm and 7mm band observations, respectively. These frequency resolutions correspond to $\sim 0.1 \text{ km s}^{-1}$ at each frequency band. We employed the spectral window mode for FOREST to cover four different lines simultaneously. The bandwidth was 63 MHz for all of the observations.

We employed the on-the-fly (OTF) observing mode (Mangum et al. 2007). In this mode, telescopes are driven smoothly and rapidly across a region of sky, while data and antenna position information are recorded continuously.

The map size is $5' \times 5'$, corresponding to 90,000 au (or $\sim 0.44 \text{ pc}$) squares at the source distance (300 pc). As we mentioned in Section 1, the origin of the streamer was not known, but the streamer comes from the north (Pineda et al. 2020). We then set the map regions covering mainly the northern part of the YSO. The separa-

rations between rows¹ were set at $6''$ and $10''$ for the 3mm and 7mm band observations.

The telescope pointing was checked every 1.5–2 hour by observing the SiO ($J = 1 - 0$) maser line from NML-Tau at $(\alpha_{J2000}, \delta_{J2000}) = (3^{\text{h}}53^{\text{m}}28\overset{\text{s}}{.}86, +11^{\circ}24'22\overset{\text{s}}{.}4)$. We used the Z45 receiver for the pointing observations. The pointing error was within $3''$.

We conducted data reduction with the NOSTAR software² provided by the Nobeyama Radio Observatory and made fits files for each line. The pixel size of the maps in the 3mm band is $8''$ and that in the 7mm band is $12''$. Baselines were calculated in line-free channels and the 1st-order polynomial fitting was applied. The velocity resolutions are 0.11 km s^{-1} for the 3mm band data and 0.15 km s^{-1} for the 7mm band data. The applied

¹ https://www.nro.nao.ac.jp/~nro45mrt/html/obs/otf/index_en.html

² https://www.nro.nao.ac.jp/~nro45mrt/html/obs/otf/reduction_en.html

convolution function was the Bessel-Gauss function. We treated the fits files generated by NOSTAR in the Common Astronomy Software Applications (CASA) package ([CASA Team et al. 2022](#)) and made maps presented in Section 3.

2.2. IRAM 30m Telescope

The observations were carried out with the IRAM 30m telescope at Pico Veleta (Spain) on 2020 May 14 and 15 under project 230-19. The EMIR E090 receiver and the FTS50 backend were employed. We used two spectral setups to cover the HC₃N (10–9) and (8–7) lines. The beam sizes were approximately 33'' and 28'' at 72 GHz and 90 GHz, respectively. We mapped a region of $\approx 150'' \times 200''$ with the OTF mode ([Mangum et al. 2007](#)). The calibration error was 10%³. Data reduction was performed using the CLASS program of the GILDAS package⁴. The beam efficiency, B_{eff} , is obtained using the Ruze formula (available in CLASS), and it is used to convert the observations into main beam temperatures, T_{mb} .

2.3. Green Bank Telescope

Observations for the Green Bank Ammonia Survey (GAS) were performed from January 2015 through March 2016 at the Robert C. Byrd Green Bank Telescope (GBT) using the 7-pixel K-band Focal Plane Array (KFPA) and the VErsatile GBT Astronomical Spectrometer (VEGAS). Observational details were first presented in GAS DR1 ([Friesen et al. 2017](#)), which focused on the NH₃ (1,1) and (2,2) emission from four regions. We refer the reader to GAS DR1 for a full description of the observations, data reduction, and imaging of the survey data.

The VEGAS backend was used in its configuration Mode 20, allowing eight spectral windows per KFPA beam, each with a bandwidth of 23.44 MHz and 4096 spectral channels. The resulting spectral resolution of 5.7 kHz gives a velocity resolution of $\sim 0.07 \text{ km s}^{-1}$ at 23.7 GHz. The GAS setup used six of eight available spectral windows to target six spectral lines in each beam, including HC₃N (5–4), and CCS (2₁ – 1₀) transition was observed in a single, central beam. In-band frequency switching with a frequency throw of 4.11 MHz was used, maximizing the observing time spent on-source.

Observations were done in OTF mode ([Mangum et al. 2007](#)), most often scanning in Right Ascension (R.A.) or Declination (Decl.) over square regions of size 10' \times

10'. The beam size was 32''. The observed coverage of most regions consists of multiple such observing blocks to cover the desired area, generally observed on different dates. Most 10' \times 10' blocks were observed once to reach the survey sensitivity goals, but several were observed twice to mitigate the effects of poor weather in the first observations. Pointing updates were usually performed in between completed maps, or more frequently if winds were high ($> 5 \text{ m s}^{-1}$). The calibration error was 10% ([Friesen et al. 2017](#)).

3. RESULTS

All of the target lines in the 3mm band (see Table 1) have been detected. The CCS ($J_N = 7_6 - 6_5$) shows low peak intensity and thus low signal-to-noise (S/N) ratios. We use another transition ($J_N = 6_7 - 5_6$) and exclude the CCS ($J_N = 7_6 - 6_5$) line from the analyses in the following sections.

In the 7mm band observations, four lines of the carbon-chain species (HC₃N, two lines of HC₅N, and CCS) have been detected, whereas CC³⁴S, *cyclic*-C₃H₂, SiO, and HNCO were not detected. The non-detection of shock tracers (SiO and HNCO) may be caused by the beam dilution effect due to the low angular resolution. We exclude these undetected lines from the following sections.

3.1. Maps of carbon-chain species

Upper panels of Figure 1 show integrated-intensity maps of (a) HC₃N ($J = 9 - 8$), (b) CCS ($J_N = 6_7 - 5_6$), and (c) CCH ($N = 1 - 0$, $J = \frac{3}{2} - \frac{1}{2}$, $F = 2 - 1$) lines in the 3mm band, and lower panels show the integrated-intensity maps of (d) HC₃N ($J = 5 - 4$), (e) CCS ($J_N = 4_3 - 3_2$), and (f) HC₅N ($J = 16 - 15$) in the 7mm band. The HC₅N ($J = 17 - 16$) line shows a similar structure to the HC₅N (16–15) line but shows weak peak intensities and low S/N ratios. We then only show the result of the HC₅N (16–15) line. We present channel maps of the three lines in the 3mm band in Figures 7–9 in Appendix A.

In panels (a) – (c) of Figure 1, we can find three structures which are labeled as (1) – (3) in panel (a); (1) associated with the YSO, (2) located at the west of the YSO, and (3) located north of the first one. The first structure corresponds to the streamer identified by [Pineda et al. \(2020\)](#). The streamer connects to the north structure, and the velocity fields show connections between the YSO and the north structure (see Figures 7–9 in Appendix A). Thus, this north structure indicated as (3) in panel (a) is the reservoir of the streamer. The diameter of the reservoir is approximately 0.04 pc, which is consistent with a typical size of starless cores (e.g.,

³ <https://www.iram.fr/GENERAL/calls/s23/30mCapabilities.pdf>

⁴ <http://www.iram.fr/IRAMFR/GILDAS>

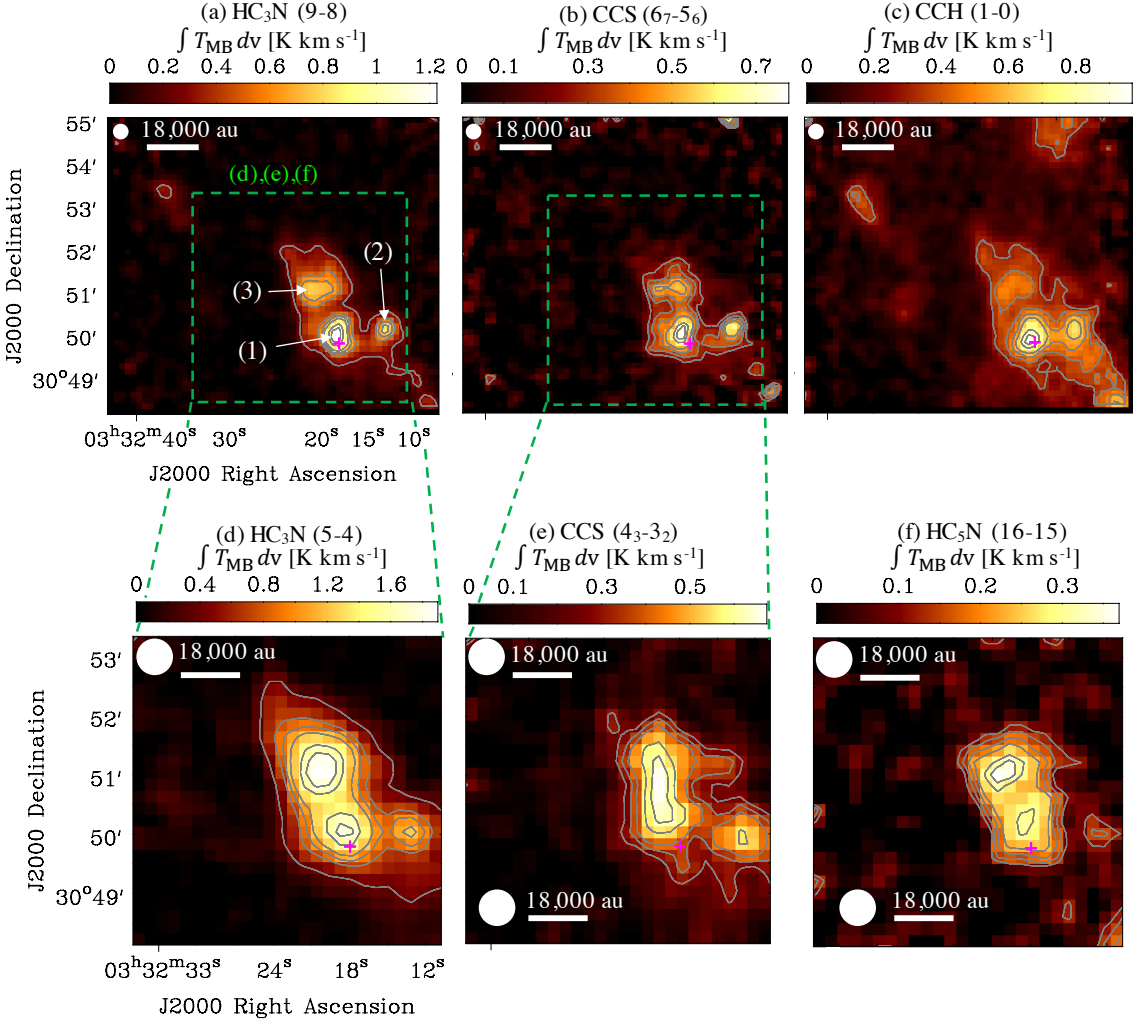


Figure 1. Integrated-intensity maps of (a) HC_3N (9 – 8), (b) CCS (67 – 56), and (c) CCH ($N = 1 - 0$, $J = \frac{3}{2} - \frac{1}{2}$, $F = 2 - 1$), (d) HC_3N (5 – 4), (e) CCS ($4_3 - 3_2$), and (f) HC_5N (16 – 15). Contour levels are relative values to their peak levels; (a, d) 20, 40, 50, 60, 80, 90 %, (b, c, f) 30, 40, 50, 60, 80, 90 %, (e) 40, 50, 60, 80, 90 %. The peak levels are (a) 1.27 K km s^{-1} , (b) 0.78 K km s^{-1} , (c) 0.97 K km s^{-1} , (d) 1.90 K km s^{-1} , (e) 0.68 K km s^{-1} , and (f) 0.37 K km s^{-1} , respectively. The integrated velocity ranges are (a) $6.1 - 8.2 \text{ km s}^{-1}$, (b) $5.9 - 7.6 \text{ km s}^{-1}$, (c) $5.6 - 8.4 \text{ km s}^{-1}$, (d) $5.8 - 8.4 \text{ km s}^{-1}$, (e) $6.1 - 8.1 \text{ km s}^{-1}$, and (f) $6.1 - 7.6 \text{ km s}^{-1}$ for each line. The noise levels of these maps are (a) 0.03 K km s^{-1} , (b) $0.047 \text{ K km s}^{-1}$, (c) 0.04 K km s^{-1} , (d) 0.03 K km s^{-1} , (e) $0.025 \text{ K km s}^{-1}$, and (f) 0.05 K km s^{-1} , respectively. The green dashed squares in panels (a) and (b) indicate the map regions of panels (d) – (f). Three identified structures are labeled as (1) – (3) in panel (a). The white-filled circles at the top left corner indicate the beam size (18'' at the 3mm and 37'' at the 7mm, respectively). The magenta cross indicates the position of the YSO.

(Pokhrel et al. 2018). The distance between the YSO and the reservoir is $\sim 20,500$ au. This reservoir is out of the Field of View (FoV) of the NOEMA observations (Pineda et al. 2020).

The three structures identified in the 3mm band data can be recognized in panels (d) HC_3N (5 – 4) and (f) HC_5N (16 – 15). On the other hand, the integrated-intensity map of the CCS ($4_3 - 3_2$) line shows a single peak between the streamer and reservoir. The west core is spatially resolved. This is probably caused by the larger beam size at 45 GHz (37'') compared to 80 GHz (18'').

3.2. Spectral analyses

We smoothed and regridded all maps to have the same beam grids as the 7mm band data obtained with the Nobeyama 45m telescope (37''). The left panel of Figure 2 shows a regridded integrated-intensity map of the HC_3N ($J = 9 - 8$) line (grayscale) overlaid with the integrated-intensity map of its $J = 5 - 4$ line (black contours). Two emission peaks, corresponding to the streamer and the reservoir, are well consistent with the two lines.

Table 2. The coordinates of Per-emb-2 YSO and emission peaks of HC₃N

| Position | R.A.(J2000) | Decl.(J2000) |
|----------|--|--------------|
| YSO | 3 ^h 32 ^m 17 ^s .96 | +30°49'47".5 |
| P1 | 3 ^h 32 ^m 20 ^s .53 | +30°51'04".5 |
| P2 | 3 ^h 32 ^m 18 ^s .68 | +30°50'03".2 |
| P3 | 3 ^h 32 ^m 13 ^s .16 | +30°50'02".6 |

We derived column densities of HC₃N, CCS, and HC₅N at the two peaks indicated as P1 and P2 in the left panel of Figure 2. The coordinates of YSO and the HC₃N emission peaks (P1 – P3) are summarized in Table 2.

3.2.1. Spectral-line energy distribution of HC₃N

We conducted the spectral-line energy distribution (SLED) analysis for the HC₃N data with the non-LTE code RADEX (van der Tak et al. 2007). The collisional parameters were obtained from Faure et al. (2016) which distinguish between *ortho*-H₂ and *para*-H₂. We searched for the best combination parameter sets to reproduce the observed integrated intensities with the least chi-square method by changing the H₂ density (n_{H_2}) and column density of HC₃N.

The line widths at each position were derived from fitting the HC₃N (9 – 8) spectra with the Gaussian profile; 0.33 km s⁻¹ and 0.65 km s⁻¹ for P1 and P2, respectively (see the right panel of Figure 2). Table 5 in Appendix B summarizes the line parameters obtained by fitting with the Gaussian profile at P1 – P3. The line widths are well consistent with the results obtained with NOEMA (see Figure 2 (b) in Pineda et al. 2020)⁵. The wider line width at P2 seems to reflect a larger velocity gradient and/or accretion shock. The velocity component at P2 is well consistent with the systemic velocity (7.05 km s⁻¹) reported by Pineda et al. (2020).

The constraints of the gas kinetic temperatures were done by the NH₃ data taken with the GBT. We fixed the gas kinetic temperature (T_{kin}) at 10 K for P1. In the case of P2, we changed T_{kin} from 13 K to 15 K with the 0.5-K step and determined it with n_{H_2} and $N(\text{HC}_3\text{N})$ simultaneously. The background temperature is fixed

at 2.73 K, the standard cosmic microwave background temperature. The tested ranges of H₂ density and HC₃N column density were 5×10^3 – 5×10^5 cm⁻³ (step is $\log(n) = 0.073$) and 5×10^{12} – 5×10^{13} cm⁻² (step is 1.8×10^{11} cm⁻²), respectively.

The results of the SLED analyses with the best parameter combinations are presented in Figure 3. The values at P1 are derived to be $n_{\text{H}_2} = (1.9 \pm 0.3) \times 10^4$ cm⁻³ and $N(\text{HC}_3\text{N}) = (2.6 \pm 0.2) \times 10^{13}$ cm⁻². For the P2 position, we determined the values of n_{H_2} , T_{kin} , and $N(\text{HC}_3\text{N})$ at $(5.1 \pm 0.6) \times 10^4$ cm⁻³, 14.5 ± 0.3 K, and $(9.4 \pm 0.2) \times 10^{12}$ cm⁻², respectively. Table 3 summarizes the obtained column densities of HC₃N at the two positions.

3.2.2. Rotational Diagram of CCS

Since there are no available collisional parameters of CCS, the SLED analysis could not be applied to the CCS lines. We have conducted the rotational diagram analysis for the CCS data. We fitted the spectra with the Gaussian profile and conducted the rotational diagram analysis in the CASSIS software (Vastel et al. 2015).

The upper panels of Figure 4 show the spectra of the three CCS lines at P1 (left) and P2 (right). Black curves indicate the results of the Gaussian fitting. The derived parameters are summarized in Table 6 in Appendix B. Line widths (FWHM) are consistent with those of HC₃N at each position. The 6₇ – 5₆ transition lines have peaks at marginally lower velocities compared to the other two lines by ~ 0.15 km s⁻¹, which may suggest that this line traces different regions due to its higher upper-state energy. However, we need high-velocity resolution data to confirm it, because our data have velocity resolutions around 0.11 – 0.15 km s⁻¹.

The lower panels of Figure 4 show the rotational diagrams at P1 (left) and P2 (right), respectively. The obtained excitation temperatures at P1 and P2, 10.5 ± 1.8 K and 13.7 ± 3.7 K, which agree with the gas kinetic temperatures derived by the SLED analysis using the HC₃N data (Section 3.2.1) within their errors. The column density at P2 is derived to be $(1.1 \pm 0.3) \times 10^{13}$ cm⁻², which is slightly higher compared to P1 ($(8.5 \pm 1.9) \times 10^{12}$ cm⁻²). Table 3 summarizes these results. We checked the optical depth (τ) of these lines in the CASSIS software by synthesizing spectra with the obtained column densities, rotational temperatures, and line widths. We confirmed that all of the lines are optically thin ($\tau \approx 0.11$ – 0.4). Thus, the rotational diagram analysis is reasonable. An optical depth of 0.4 may cause an underestimation of the column density at most 20%, which is smaller than the fitting errors (~ 22 – 27%).

⁵ The relationship between FWHM and σ is as follows: FWHM = $2\sigma\sqrt{2\ln 2}$.

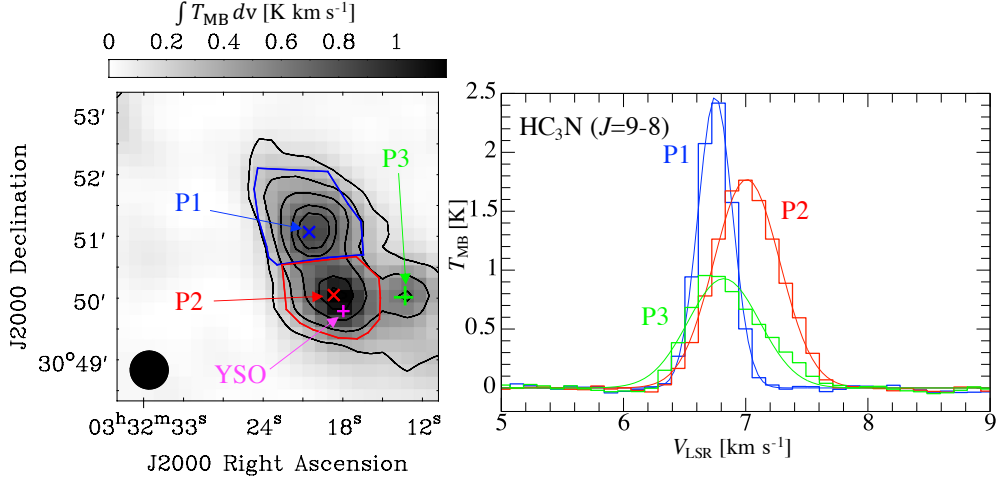


Figure 2. Left panel shows a regridded integrated-intensity map of HC_3N ($J = 9 - 8$) overlaid with contours indicating the HC_3N ($J = 5 - 4$) line (contour levels are 20, 40, 60, 80, 90% of the peak intensity). Two crosses (P1 and P2) indicate two positions where we conducted spectral analyses. The polygons harboring P1 and P2 indicate the regions where we derived the mass. The green cross indicated as P3 is the other emission peak. The magenta cross indicates the position of the YSO. Right panel shows spectra of the HC_3N ($J = 9 - 8$) line at P1 (blue), P2 (red), and P3 (green) respectively. The curves show fitting results with the Gaussian profile. The fitting parameters are summarized in Table 5 in Appendix B.

Table 3. Results of line analyses

| Species | Analytical Method | P1 | | P2 | |
|-----------------------|--------------------|--------------------------------|---------------------|--------------------------------|---------------------|
| | | N (cm^{-2}) | T_{ex} (K) | N (cm^{-2}) | T_{ex} (K) |
| HC_3N | SLED | $(2.6 \pm 0.2) \times 10^{13}$ | ... | $(9.4 \pm 0.2) \times 10^{12}$ | ... |
| CCS | Rotational Diagram | $(8.5 \pm 1.9) \times 10^{12}$ | 10.5 ± 1.8 | $(1.1 \pm 0.3) \times 10^{13}$ | 13.7 ± 3.7 |
| HC_5N | MCMC | $(8.9 \pm 0.9) \times 10^{12}$ | 10.7 ± 0.7 | $(9.5 \pm 0.9) \times 10^{12}$ | 13.03 ± 0.03 |

NOTE—The errors indicate the standard deviation.

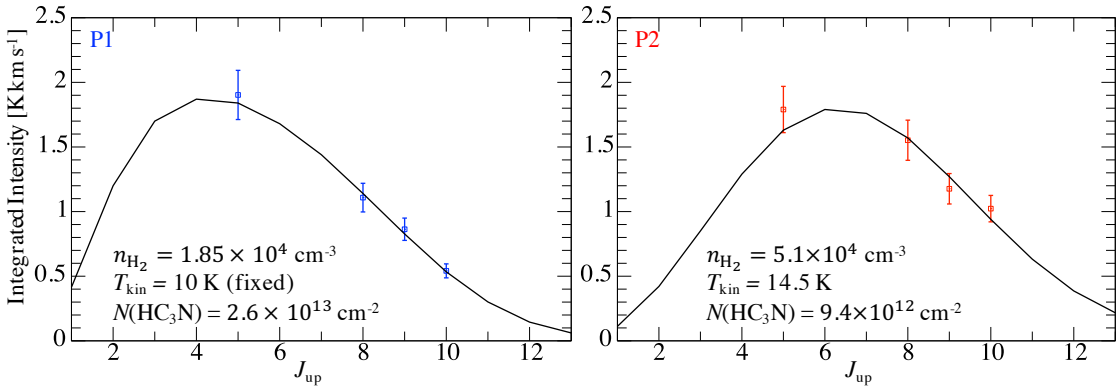


Figure 3. Results of the SLED analysis with HC_3N lines toward P1 (left) and P2 (right). The blue and red points indicate the observed values. The 10% errors due to a typical uncertainty of the chopper-wheel method are taken into consideration. The black curves indicate the best fitting result with the parameters shown in each panel; $n_{\text{H}_2} = 1.85 \times 10^4 \text{ cm}^{-3}$, $T_{\text{kin}} = 10 \text{ K}$ (fixed) and $N(\text{HC}_3\text{N}) = 2.6 \times 10^{13} \text{ cm}^{-2}$ for P1, and $n_{\text{H}_2} = 5.1 \times 10^4 \text{ cm}^{-3}$, $T_{\text{kin}} = 14.5 \text{ K}$, and $N(\text{HC}_3\text{N}) = 9.4 \times 10^{12} \text{ cm}^{-2}$ for P2, respectively.

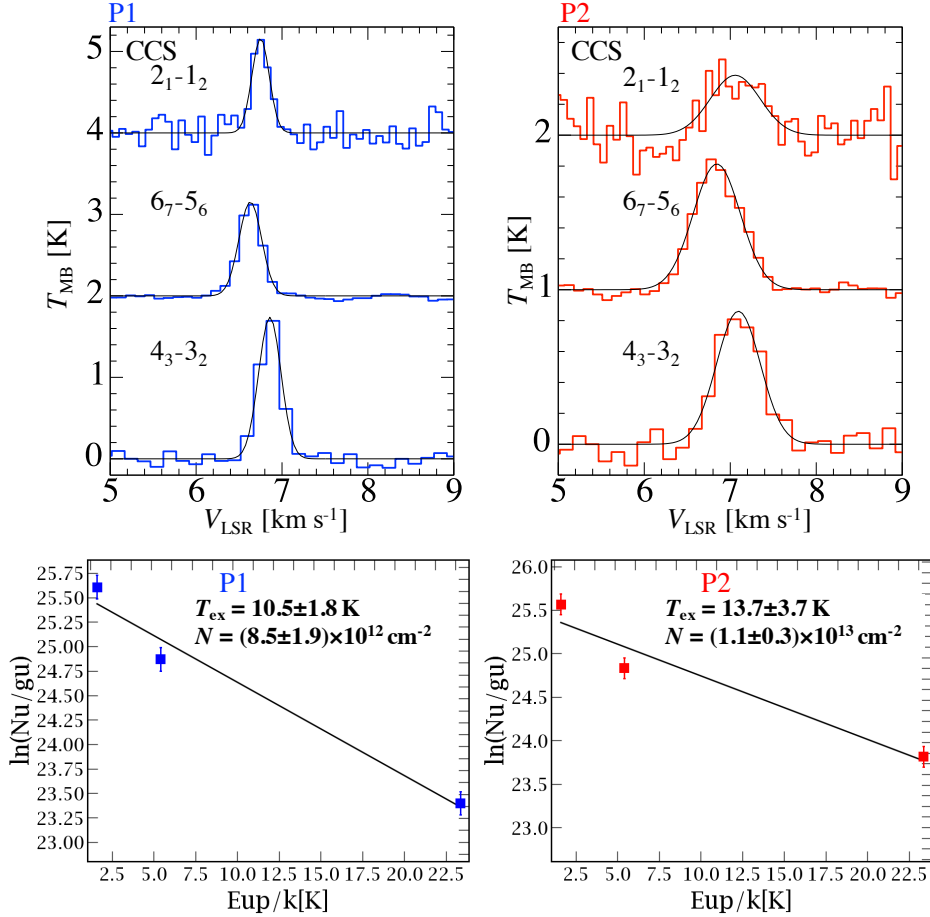


Figure 4. Upper panels show CCS spectra of the three transitions at P1 (left) and P2 (right). Blue and red lines indicate the observed spectra, and black curves indicate the results of the Gaussian fitting. Lower panels show rotational diagrams of the CCS lines at P1 (left) and P2 (right), respectively. Errors are calculated from the Gaussian fitting errors and the calibration errors (10%).

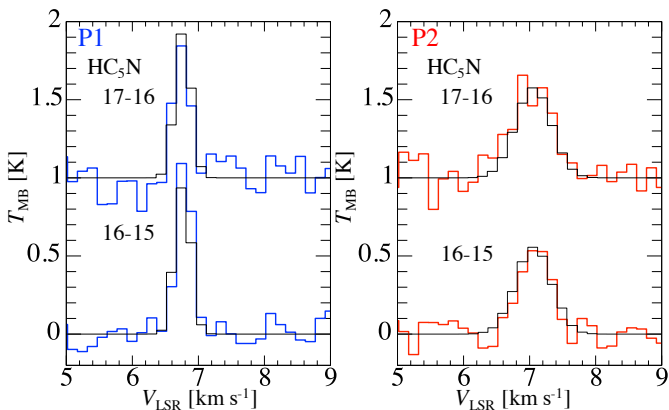


Figure 5. Two HC_5N spectra at P1 (left) and P2 (right) overlaid by the best fitting results obtained by the MCMC method (black lines).

Hence, we conclude that the optical thickness does not affect our results significantly.

3.2.3. Markov Chain Monte Carlo of HC_5N

As we have two HC_5N lines with similar upper-state energies, the rotational diagram method could not be applied. We analyzed the HC_5N spectra with the Markov Chain Monte Carlo (MCMC) method assuming the local thermodynamic equilibrium (LTE) condition in the CASSIS software (Vastel et al. 2015). The critical density of the HC_5N line is $\sim 10^4 \text{ cm}^{-3}$ (Hirota et al. 2009; Taniguchi et al. 2016), which is similar to the H_2 densities at P1 and P2, and then the LTE assumption is reasonable here.

The column density (N), excitation temperature (T_{ex}), velocity component of the line peak (V_{LSR}), and line width (FWHM) were treated as free parameters. We constrained the excitation temperatures at $9.5 - 12.0 \text{ K}$ and $10.0 - 15.0 \text{ K}$ at P1 and P2, respectively (see Sections 3.2.1 and 3.2.2). The tested ranges of FWHM and V_{LSR} were $0.1 - 0.8 \text{ km s}^{-1}$ and $6.0 - 7.5 \text{ km s}^{-1}$ at P1, and $0.1 - 1.6 \text{ km s}^{-1}$ and $6.4 - 7.5 \text{ km s}^{-1}$ at P2. The range of the column density was $2.0 \times 10^{12} - 8.0 \times 10^{13} \text{ cm}^{-2}$ at both P1 and P2. Since the emission size is much larger than the beam size ($37''$), the beam dilution effect does not affect the analysis.

Blue and red lines in Figure 5 show the observed spectra of two HC_5N lines at P1 (left) and P2 (right). The black lines indicate the best-fitting model for each spectrum. The optical depths are $\sim 0.30 - 0.33$ and $\sim 0.093 - 0.095$ at P1 and P2, respectively. Thus, the assumption of the LTE is reasonable.

Table 3 summarizes derived column densities and excitation temperatures at each position. The derived FWHM and V_{LSR} are $0.28 \pm 0.02 \text{ km s}^{-1}$ and $7.65 \pm 0.008 \text{ km s}^{-1}$ at P1, and $0.63 \pm 0.03 \text{ km s}^{-1}$ and

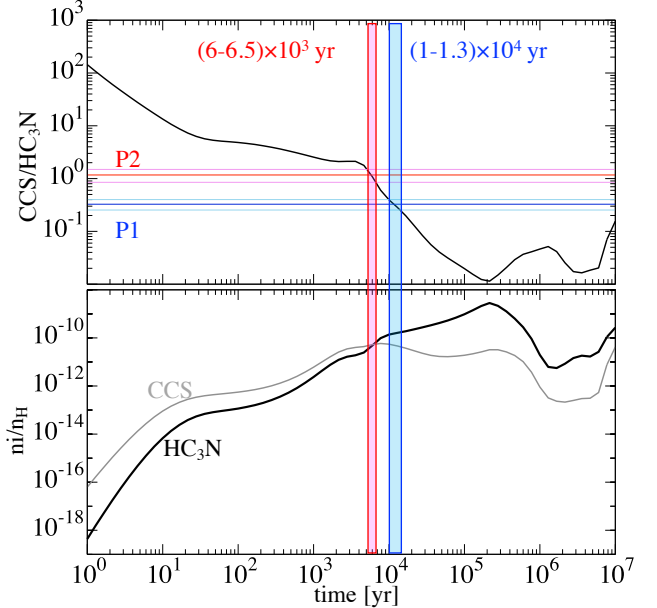


Figure 6. The upper panel shows comparisons of the observed CCS/ HC_3N abundance ratios at P1 and P2 to the modeled results. The horizontal lines show the observed values (light-colored lines indicate the upper and lower limits). The lower panel shows abundances of HC_3N (black) and CCS (gray). The shaded vertical regions indicate the best-fit ages.

$7.06 \pm 0.02 \text{ km s}^{-1}$ at P2, respectively. These line widths (FWHM) are consistent with those of HC_3N and CCS, and the velocity components match with those of HC_3N at each position (see Tables 5 and 6 in Appendix B).

4. DISCUSSION

We derive masses of the reservoir (P1) and the streamer (P2). Blue and red polygons in the left panel of Figure 2 indicate regions where masses are derived. Hereafter, we call them “Region P1” and “Region P2”, respectively.

4.1. Comparisons with chemical simulation

We ran chemical simulations with a constant temperature and density model utilized for starless cores (Taniguchi et al. 2019) to constrain the HC_3N abundances from the CCS/ HC_3N abundance ratios. We used the gas-grain Nautilus code (Ruaud et al. 2016). The temperature and density are fixed at 10 K and 10^4 cm^{-3} , respectively. This condition is constrained by the results of the SLED analyses (Section 3.2.1). The P1 position corresponds to the emission peak of carbon-chain species, and the density at P1 is likely higher compared to the environments. Since the density and temperature do not change drastically between P1 and P2, this assumption is reasonable for most of the gas within these regions.

We applied the three-phase model, in which the chemistry of the gas phase, the grain surface, and the bulk ice are treated. We applied the cosmic-ray ionization rate of $1.3 \times 10^{-17} \text{ s}^{-1}$. All of the parameters are the same as in the chemical code described in Taniguchi et al. (2019), which is used for the chemical simulations of starless cores in nearby low-mass star-forming regions.

We compared the CCS/HC₃N abundance ratios at P1 and P2 to the chemical model (upper panel of Figure 6). The observed CCS/HC₃N abundance ratios at P1 and P2 are 0.33 ± 0.07 and 1.2 ± 0.3 , respectively. Table 4 summarizes the best-fit ages and the HC₃N abundances at the best-fit ages (see the lower panel of Figure 6) at P1 and P2. The best-fit ages are $(1 - 1.3) \times 10^4 \text{ yr}$ and $(6 - 6.5) \times 10^3 \text{ yr}$ at P1 and P2, respectively. The different ages at P1 and P2 positions may be caused by different emission regions for HC₃N and CCS. Since the critical densities of the HC₃N ($5 - 4$) and CCS ($4_3 - 3_2$) lines are more or less similar ($n_{\text{H}_2} \approx 10^{4-5} \text{ cm}^{-3}$; Dobashi et al. 2018), these two lines are expected to trace similar regions. Here, we simply assume that both lines trace the same regions. However, integrated-intensity maps of these two lines in the 7mm band (panels (d) and (e) of Figure 1) show different features. This may be caused by the low angular resolution, but we could not completely exclude the possibility that these lines trace slightly different regions.

We also conducted the same analysis using the CCS/HC₅N abundance ratios as shown in the upper panel of Figure 10 in Appendix C. The best-fit ages are around $(2.3 - 3.0) \times 10^4 \text{ yr}$ at P1 and P2. Thus, P1 and P2 have chemically young characteristics such that carbon-chain species are abundant (see the lower panel of Figure 10 in Appendix C).

Pineda et al. (2020) found that the emission of N₂H⁺ and its deuterium species do not trace the streamer. This is explained by the fact that the streamer brings in chemically fresh gas. We checked this point with the results of the chemical model. The lower panel of Figure 10 in Appendix C shows the time evolution of abundances of the three carbon-chain species (CCS, HC₃N, HC₅N) and N₂H⁺. Around 10^4 yr , the abundance of N₂H⁺ ($\sim 10^{-13}$) is lower than those of the carbon-chain species by more than two orders of magnitude. Thus, the streamer cannot be traced by the N₂H⁺ lines as the observations showed (Pineda et al. 2020).

All of the results agree that the reservoir and the streamer have chemically young characteristics, and their chemical ages are very similar. This is other evidence that Region P1 is the origin of the streamer, *i.e.*, the reservoir.

Table 4. Summary of results from comparisons with chemical simulations

| Parameters | P1 | P2 |
|-------------------------------------|--------------------------------|-------------------------------|
| Age [yr] | $(1 - 1.3) \times 10^4$ | $(5 - 6.5) \times 10^3$ |
| $X(\text{HC}_3\text{N})$ | $(1.38 - 1.7) \times 10^{-10}$ | $(3 - 7) \times 10^{-11}$ |
| $N(\text{H}_2)$ [cm ⁻²] | $(7.7 - 9.5) \times 10^{22}$ | $(6.7 - 11.8) \times 10^{22}$ |
| Region mass [M _⊙] | 14.5 – 17.9 | 9.3 – 16.2 |

4.2. Masses of the reservoir and the streamer

Using the HC₃N column densities (see Table 3 and Section 3.2.1) and its constrained abundances at P1 and P2 (Table 4), we derived the H₂ column densities, denoted as $N(\text{H}_2)$, at P1 and P2⁶. The $N(\text{H}_2)$ values are derived to be $(7.7 - 9.5) \times 10^{22} \text{ cm}^{-2}$ and $(6.7 - 11.8) \times 10^{22} \text{ cm}^{-2}$ at P1 and P2, respectively (Table 4).

We derived masses of Region P1 and Region P2 within the blue and red polygons in the left panel of Figure 2. The masses within Region P1 (the reservoir; M_{Region1}) and Region P2 (the streamer; M_{Region2}) are derived to be $14.5 - 17.9 \text{ M}_{\odot}$ and $9.3 - 16.2 \text{ M}_{\odot}$, respectively. Thus, the total mass available for the streamer is $24 - 34 \text{ M}_{\odot}$.

Pineda et al. (2020) derived the mass of the streamer to be 0.1 M_{\odot} , and their results underestimated the mass of the streamer. This is caused by the fact that they assumed a very high HC₃N abundance ([HC₃N]/[H₂] = 7.4×10^{-9}), which is comparable to that at the Cyanopolyyne Peak in Taurus Molecular Cloud-1 where carbon-chain molecules are extraordinarily abundant (e.g., Suzuki et al. 1992; Kaifu et al. 2004; Dobashi et al. 2018). Their applied value is higher than those we derived by two orders of magnitude. In addition, we calculated the masses within larger areas compared to Pineda et al. (2020). These differences cause the different derived masses between the two studies. The reservoir (Region P1), which was not covered by the previous NOEMA observations (Pineda et al. 2020), harbors gas that is comparable to or more abundant than the streamer.

4.3. How long will mass accretion last via the streamer?

To evaluate the lifetime of the streamer, we first calculate the streamer infall rate ($\dot{M}_{\text{streamer}}$). There is a possibility that Region P2 contains gas outside of the

⁶ $N(\text{H}_2) = N(\text{HC}_3\text{N})/2X(\text{HC}_3\text{N})$

streamer which will not eventually flow into the protostellar system. To investigate this possibility, we calculated the mass of the streamer using the following formulae:

$$M_{\text{new}} = M_{\text{Pineda}} \frac{X_{\text{Pineda}}}{X_{\text{P2}}}. \quad (1)$$

M_{Pineda} ($= 0.1 \text{ M}_\odot \text{ yr}^{-1}$) is the mass of the streamer derived by Pineda et al. (2020). X_{Pineda} ($= 3.95 \times 10^{-9}$, which was converted into the value concerning the total hydrogen nuclei) is the HC_3N abundance assumed in Pineda et al. (2020), and X_{P2} ($= (3 - 7) \times 10^{-11}$) means the HC_3N abundance, $X(\text{HC}_3\text{N})$, at P2 (Table 4). Using this formula, we obtained $5.6 - 13.2 \text{ M}_\odot$ for the mass of the streamer. Hence, the gas mass within Region P2 ($9.3 - 16.2 \text{ M}_\odot$) is higher than the newly calculated value by a factor of ~ 1.4 . This means that the single-dish observations trace gas from mostly the streamer, but small contamination from the extended gas is present.

To derive the streamer infall rate, we thus used the following formulae utilizing the result of Pineda et al. (2020) which only covers the streamer:

$$\dot{M}_{\text{streamer}} = \dot{M}_{\text{Pineda}} \frac{X_{\text{Pineda}}}{X_{\text{P2}}}, \quad (2)$$

where \dot{M}_{Pineda} ($= 10^{-6} \text{ M}_\odot \text{ yr}^{-1}$) is the streamer infall rate derived by Pineda et al. (2020). The newly calculated streamer infall rate is $(5.6 - 13.2) \times 10^{-5} \text{ M}_\odot \text{ yr}^{-1}$.

With the newly obtained streamer infall rate, we calculated the lifetime of the streamer (t_L). We assumed that all of the gas in Region P1 would continue to accrete onto the YSO with the current streamer infall rate and would not go to the ambient components. We estimated the lifetime of the streamer with the following formulae:

$$t_L = \frac{M_{\text{Region1}}}{\dot{M}_{\text{streamer}}}, \quad (3)$$

where M_{Region1} corresponds to the mass within Region P1 ($14.5 - 17.9 \text{ M}_\odot$). With the above assumption, the derived lifetime is $(1.1 - 3.2) \times 10^5 \text{ yr}$, corresponding to a factor of $1.1 - 3.3$ of the free-fall timescale (96 kyr; Pineda et al. 2020). Considering the typical evolution of YSOs (Dauphas & Chaussidon 2011; Dunham et al. 2014), mass accretion via the streamer will be able to continue until the end of the Class I stage.

Region P1 (the reservoir) is likely a starless core, but it may not be able to form a new protostar, because the material within this region is flowing into the Per-emb-2 protostellar system. Note that Region P1 would chemically evolve, and the best tracers of the streamer may change with time.

A possible reason why the YSO Per-emb-2 is deficient in COMs (Yang et al. 2021) may be that the chemically

young gas has been brought from another starless-core-like region and changed the chemical composition near the protostellar core. To confirm this, we need high-angular-resolution observations to investigate chemical differentiation among carbon-chain species and CH_3OH around the YSO.

The P3 position may be an extra reservoir of material that contributes to the mass accretion into the YSO Per-emb-2, although we cannot measure an accretion rate from P3 due to the low-angular-resolution data. The P3 position has the almost same centroid velocities as P1 (see Figure 2 and Table 5), suggesting that they trace the same cloud material around P2, while P2 shows the red-shifted components that is the line-of-sight motion of material from the cloud toward the protostar. The line width at P2 is more similar to that at P3 (Table 5), which suggests that accretion of material from P3 may currently be, or has been in the past, dominant. Another possibility for the wide line widths at P2 is that the turbulence is caused by the protostellar activity. We need high-angular-resolution observations covering P2 and P3 to clarify contributions from P3.

5. CONCLUSIONS

We conduct mapping observations of four carbon-chain species (HC_3N , HC_5N , CCH, and CCS) in the 3mm and 7mm bands toward the Per-emb-2 streamer in the Perseus region with the Nobeyama 45m radio telescope. The main conclusions of this paper are as follows.

1. We find a structure at the north part of the protostellar system with a distance of $\sim 20,500 \text{ au}$ in integrated-intensity maps of the carbon-chain species. This structure connects to the streamer and is identified as the reservoir of the streamer.
2. Combining the data obtained by the IRAM 30m telescope, we conduct the spectral-line energy distribution (SLED) analysis with the non-LTE RADEX code and the HC_3N lines. We derive the density at the HC_3N emission peak within the reservoir (P1 position) $n_{\text{H}_2} = (1.9 \pm 0.3) \times 10^4 \text{ cm}^{-3}$ with the gas kinetic temperature of 10 K. The position where the streamer connects to the YSO (P2 position) shows a slightly higher temperature and density; 14.5 K and $(5.1 \pm 0.6) \times 10^4 \text{ cm}^{-3}$. The streamer system has likely almost homogeneous density and temperature structures.
3. We compare the observed CCS/ HC_3N abundance ratios to the chemical model and constrain the relative abundances of HC_3N to the hydrogen nuclei. P1 and P2 are chemically young ($t \approx 10^4 \text{ yr}$). This

agrees with the fact that the Per-emb-2 streamer is well traced by carbon-chain species, whereas the emission of N_2H^+ is not consistent with the streamer structure (Pineda et al. 2020). Moreover, similar chemical compositions at P1 and P2 strengthen our conclusion that Region P1 is the reservoir of the streamer.

4. The derived masses of the reservoir and the streamer are $\sim 14.5 - 18 \text{ M}_\odot$ and $\sim 9 - 16 \text{ M}_\odot$, respectively. Thus, the total mass available for the streamer is determined at $24 - 34 \text{ M}_\odot$.
5. The streamer infall rate is recalculated at $(5.6 - 13.2) \times 10^{-5} \text{ M}_\odot \text{ yr}^{-1}$. We estimate the lifetime of the streamer assuming that all of the gas in the reservoir will flow into the Per-emb-2 protostellar system. The lifetime is calculated to be $(1.1 - 3.2) \times 10^5 \text{ yr}$. The value exceeds the free-fall timescale by a factor of $1.1 - 3.3$. The results suggest that the mass accretion via the streamer can continue until the end of the Class I phase.

Streamers have been found by observations with interferometries toward YSOs at various evolutionary stages. We demonstrate that single-dish mapping observations are also important to find out the origin(s) of streamers and derive their total masses.

APPENDIX

A. CHANNEL MAPS OF CARBON-CHAIN SPECIES IN THE 3MM BAND

Figures 7, 8, and 9 show channel maps of the HC_3N ($J = 9 - 8$), CCS ($J_N = 6_7 - 5_6$), and CCH ($N = 1 - 0$, $J = \frac{3}{2} - \frac{1}{2}$, $F = 2 - 1$) lines, respectively. Velocity gradients from the northern part to the YSO can be seen in these channel maps. All of the three molecular lines show similar structures. The upper-state energy of the CCH line is lower than those of the other two species (Table 1). This explains the more extended morphology of CCH (1-0) compared to the other lines.

B. GAUSSIAN FITTING RESULTS OF HC_3N AND CCS LINES

Table 5 summarizes line parameters obtained by the Gaussian fitting of the HC_3N ($J = 9 - 8$) line at P1, P2, and P3. The right panel of Figure 2 shows the observed spectra overlaid by these Gaussian fitting results.

We would like to express thanks to the staff of the Nobeyama Radio Observatory. The Nobeyama 45m radio telescope is operated by Nobeyama Radio Observatory, a branch of National Astronomical Observatory of Japan. K.T. is supported by JSPS KAKENHI grant No. JP20K14523 and 21H01142. K.T. is grateful for research funds for NAOJ Fellow to purchase the observing time of the Nobeyama 45m radio telescope and to support with travel funding for visiting Max-Planck-Institut für Extraterrestrische Physik (MPE). K.T. greatly appreciates NAOJ Overseas Visit Program for Young Researchers 2023 for support with travel funding for visiting MPE. T.S. has been financially supported by JSPS KAKENHI grant No. 22K02966 and the Kayamori Foundation of Informational Science Advancement. DMS is supported by an NSF Astronomy and Astrophysics Postdoctoral Fellowship under award AST-2102405. We appreciate an anonymous referee whose comments are helpful to improve the paper.

Facilities: Nobeyama 45m radio telescope

Software: Common Astronomy Software Applications package (CASA; CASA Team et al. 2022), CASSIS (Vastel et al. 2015), Nautilus (Ruaud et al. 2016)

Table 5. Line parameters of the HC_3N ($J = 9 - 8$) line

| Position | T_{MB} (K) | V_{LSR} (km s^{-1}) | FWHM (km s^{-1}) |
|----------|---------------------|---|-----------------------------|
| P1 | 2.47 ± 0.02 | 6.751 ± 0.001 | 0.331 ± 0.003 |
| P2 | 1.77 ± 0.02 | 7.009 ± 0.004 | 0.65 ± 0.01 |
| P3 | 0.93 ± 0.03 | 6.82 ± 0.01 | 0.69 ± 0.03 |

NOTE—The errors indicate the standard deviation.

Table 6 summarizes line parameters of the CCS lines at P1 and P2 obtained by fitting with the Gaussian profile. The spectra with the results of the Gaussian fitting are shown in the upper panels of Figure 4.

C. COMPARISONS OF THE CCS/ HC_5N ABUNDANCE RATIOS

The upper panel of Figure 10 shows the comparisons between the observed CCS/ HC_5N ratios at P1 and P2 to the modeled one. The observed ratios are 0.98 ± 0.23 and 1.16 ± 0.34 at P1 and P2, respectively. Their

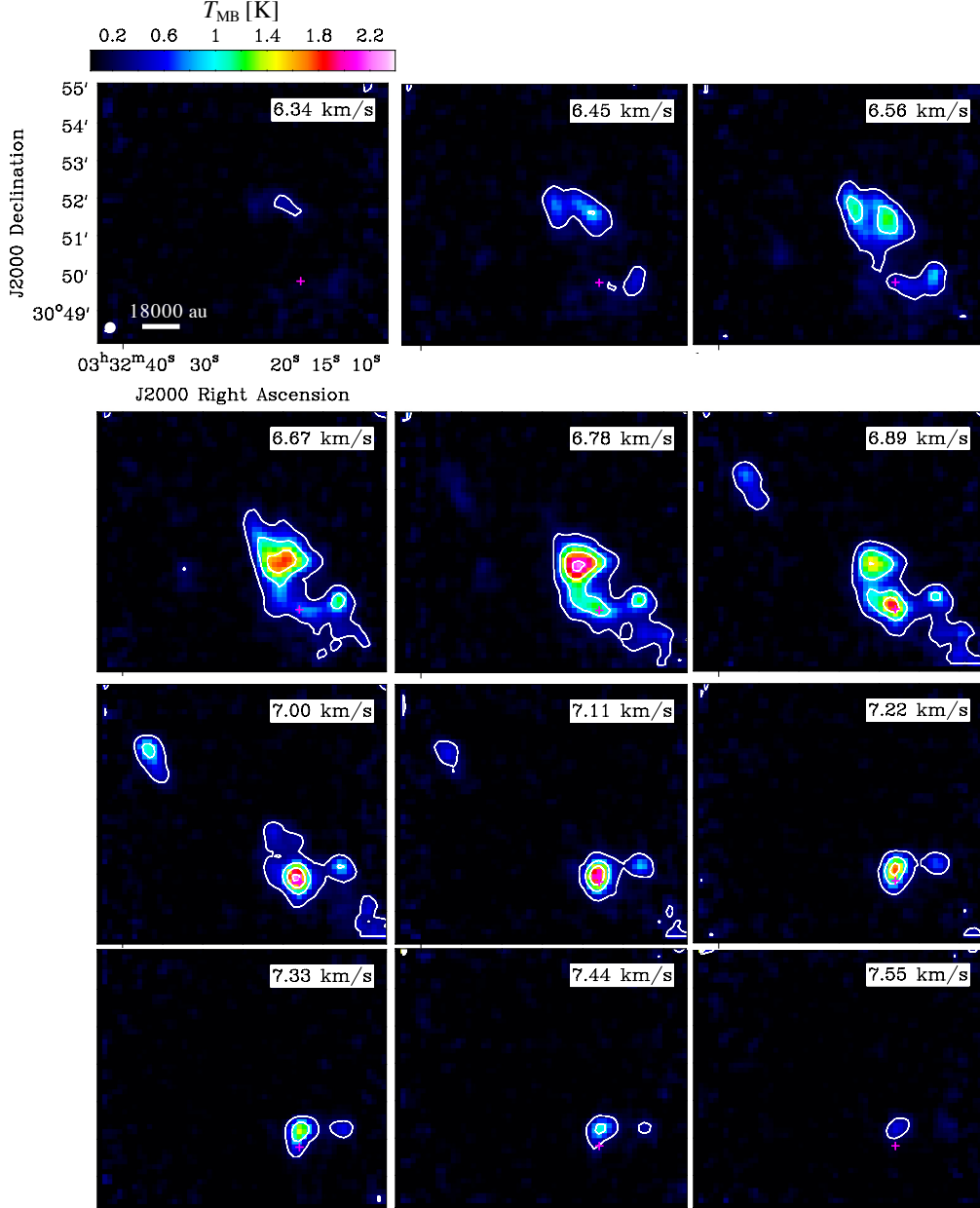


Figure 7. Channel maps of the HC_3N ($J = 9 - 8$) line. The magenta cross indicates the position of the YSO. The contour levels are 10, 30, 50, 70σ , where $\sigma = 0.03 \text{ K}$. The white-filled circle at the bottom left corner in the first panel indicates the beam size at 80 GHz ($18''$).

relative abundances agree with each other within their uncertainties. The best-fit ages at P1 and P2 are almost the same age of $(2.3 - 3.0) \times 10^4 \text{ yr}$. This is close to the best agreement age obtained from the comparisons of CCS/ HC_3N ratios.

The lower panel of Figure 10 shows the time evolution of molecular abundances of the three carbon-chain species and N_2H^+ . The abundance of N_2H^+ around 10^4 yr is below 10^{-13} , which is lower than those of carbon-chain species by more than two orders of magnitude.

REFERENCES

Alves, F. O., Caselli, P., Girart, J. M., et al. 2019, Science,

366, 90. doi:10.1126/science.aaw3491

Arzoumanian, D., Arakawa, S., Kobayashi, M. I. N., et al.

2023, ApJL, 947, L29. doi:10.3847/2041-8213/acc849

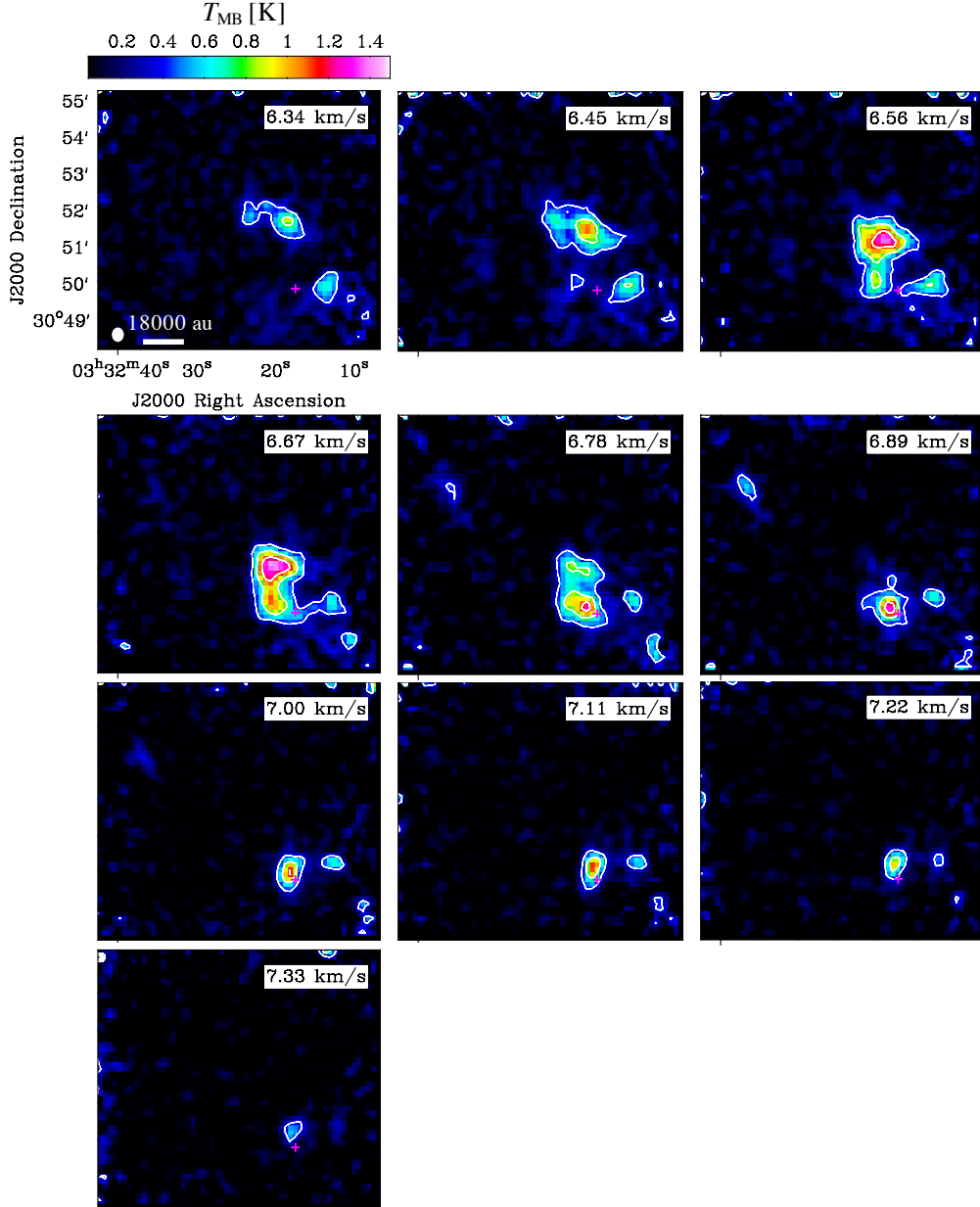


Figure 8. Channel maps of the CCS ($J_N = 6_7 - 5_6$) line. The magenta cross indicates the position of the YSO. The contour levels are 10, 20, 30σ , where $\sigma = 0.038$ K. The white-filled circle at the bottom left corner in the first panel indicates the beam size at 80 GHz (18'').

Benson, P. J., Caselli, P., & Myers, P. C. 1998, ApJ, 506, 743. doi:10.1086/306276

Bate, M. R. 2018, MNRAS, 475, 5618. doi:10.1093/mnras/sty169

CASA Team, Bean, B., Bhatnagar, S., et al. 2022, PASP, 134, 114501. doi:10.1088/1538-3873/ac9642

Chou, H.-G., Yen, H.-W., Koch, P. M., et al. 2016, ApJ, 823, 151. doi:10.3847/0004-637X/823/2/151

Cuello, N., Louvet, F., Mentiplay, D., et al. 2020, MNRAS, 491, 504. doi:10.1093/mnras/stz2938

Dauphas, N. & Chaussidon, M. 2011, Annual Review of Earth and Planetary Sciences, 39, 351.

doi:10.1146/annurev-earth-040610-133428

Dobashi, K., Shimoikura, T., Nakamura, F., et al. 2018, ApJ, 864, 82. doi:10.3847/1538-4357/aad62f

Dunham, M. M., Stutz, A. M., Allen, L. E., et al. 2014, Protostars and Planets VI, 195.

doi:10.2458/azu_uapress_9780816531240-ch009

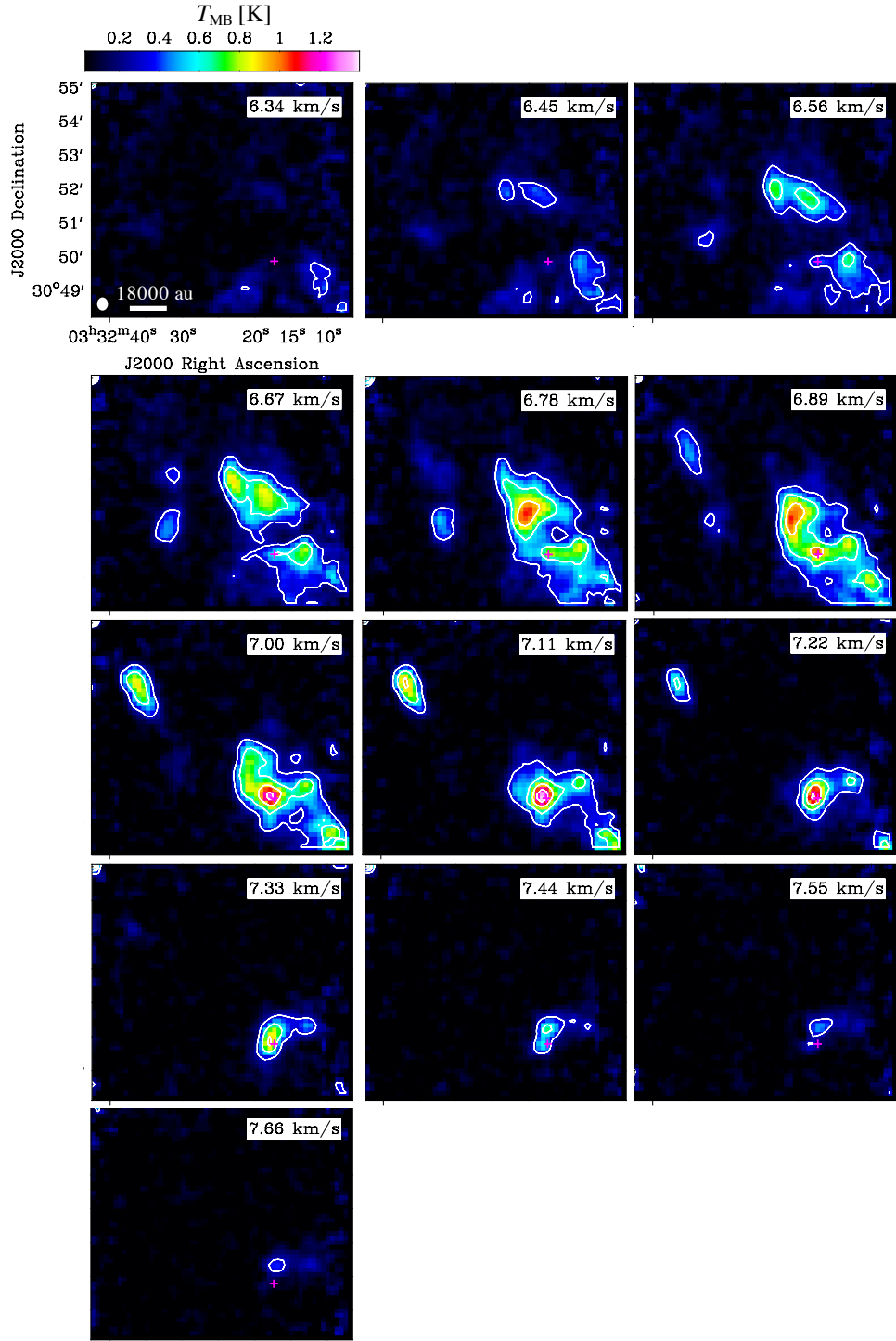


Figure 9. Channel maps of the CCH ($N = 1 - 0$, $J = \frac{3}{2} - \frac{1}{2}$, $F = 2 - 1$) line. The magenta cross indicates the position of the YSO. The contour levels are $10, 20, 30, 40\sigma$, where $\sigma = 0.03$ K. The white-filled circle at the bottom left corner in the first panel indicates the beam size at 80 GHz ($18''$).

Table 6. Line parameters of the CCS lines

| Transition | P1 | | | P2 | | |
|-------------|---------------------|---|-----------------------------|---------------------|---|-----------------------------|
| | T_{MB} (K) | V_{LSR} (km s^{-1}) | FWHM (km s^{-1}) | T_{MB} (K) | V_{LSR} (km s^{-1}) | FWHM (km s^{-1}) |
| $4_3 - 3_2$ | 1.74 ± 0.06 | 6.858 ± 0.005 | 0.322 ± 0.012 | 0.86 ± 0.05 | 7.095 ± 0.018 | 0.60 ± 0.04 |
| $6_7 - 5_6$ | 1.15 ± 0.02 | 6.631 ± 0.003 | 0.311 ± 0.007 | 0.813 ± 0.019 | 6.844 ± 0.007 | 0.645 ± 0.017 |
| $2_1 - 1_2$ | 1.16 ± 0.12 | 6.750 ± 0.012 | 0.24 ± 0.03 | 0.39 ± 0.06 | 7.06 ± 0.05 | 0.68 ± 0.13 |

NOTE—The errors indicate the standard deviation.

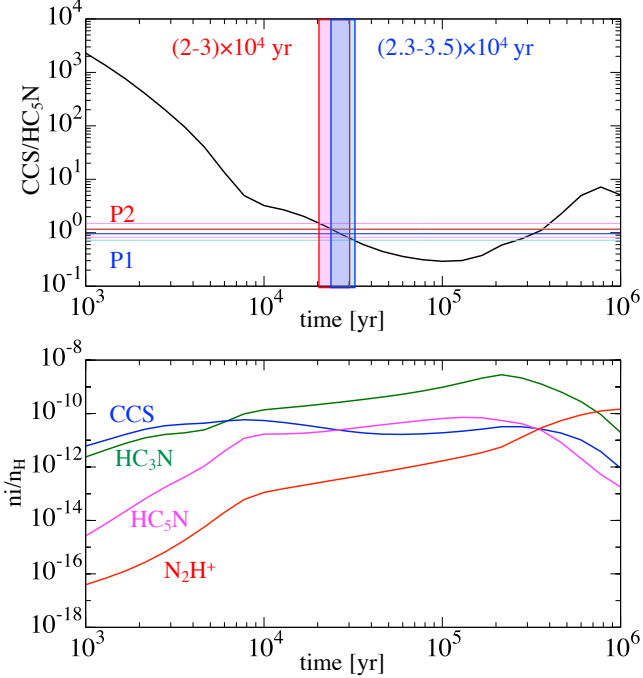


Figure 10. The upper panel compares the observed abundance ratios of CCS/HC₅N at P1 and P2 to the modeled ones. The horizontal lines show the observed values (light-colored lines indicate the upper and lower limits). The lower panels show the abundances of three carbon-chain species and N₂H⁺.

- Endres, C. P., Schlemmer, S., Schilke, P., et al. 2016, Journal of Molecular Spectroscopy, 327, 95. doi:10.1016/j.jms.2016.03.005
Faure, A., Lique, F., & Wiesenfeld, L. 2016, MNRAS, 460, 2103. doi:10.1093/mnras/stw1156
Fernández-López, M., Girart, J. M., López-Vázquez, J. A., et al. 2023, ApJ, 956, 82. doi:10.3847/1538-4357/ace786
Friesen, R. K., Pineda, J. E., co-PIs, et al. 2017, ApJ, 843, 63. doi:10.3847/1538-4357/aa6d58
Garufi, A., Podio, L., Codella, C., et al. 2022, A&A, 658, A104. doi:10.1051/0004-6361/202141264
Ginski, C., Facchini, S., Huang, J., et al. 2021, ApJL, 908, L25. doi:10.3847/2041-8213/abdf57
Hirota, T., Ohishi, M., & Yamamoto, S. 2009, ApJ, 699, 585. doi:10.1088/0004-637X/699/1/585
Hsieh, T.-H., Segura-Cox, D. M., Pineda, J. E., et al. 2023, A&A, 669, A137. doi:10.1051/0004-6361/202244183
Kaifu, N., Ohishi, M., Kawaguchi, K., et al. 2004, PASJ, 56, 69. doi:10.1093/pasj/56.1.69
Kamazaki, T., Okumura, S. K., Chikada, Y., et al. 2012, PASJ, 64, 29. doi:10.1093/pasj/64.2.29
Le Gouellec, V. J. M., Hull, C. L. H., Maury, A. J., et al. 2019, ApJ, 885, 106. doi:10.3847/1538-4357/ab43c2

- Lee, J.-E., Matsumoto, T., Kim, H.-J., et al. 2023, ApJ, 953, 82. doi:10.3847/1538-4357/acdd5b
Mangum, J. G., Emerson, D. T., & Greisen, E. W. 2007, A&A, 474, 679. doi:10.1051/0004-6361:20077811
Mottram, J. C., van Dishoeck, E. F., Kristensen, L. E., et al. 2017, A&A, 600, A99. doi:10.1051/0004-6361/201628682
Müller, H. S. P., Schlöder, F., Stutzki, J., et al. 2005, Journal of Molecular Structure, 742, 215. doi:10.1016/j.molstruc.2005.01.027
Minamidani, T., Nishimura, A., Miyamoto, Y., et al. 2016, Proc. SPIE, 9914, 99141Z. doi:10.1117/12.2232137
Murillo, N. M., van Dishoeck, E. F., Hacar, A., et al. 2022, A&A, 658, A53. doi:10.1051/0004-6361/202141250
Nakamura, F., Ogawa, H., Yonekura, Y., et al. 2015, PASJ, 67, 117. doi:10.1093/pasj/psv088
Pickett, H. M., Poynter, R. L., Cohen, E. A., et al. 1998, JQSRT, 60, 883. doi:10.1016/S0022-4073(98)00091-0
Pineda, J. E., Arzoumanian, D., Andre, P., et al. 2023, Protostars and Planets VII, 534, 233. doi:10.48550/arXiv.2205.03935
Pineda, J. E., Segura-Cox, D., Caselli, P., et al. 2020, Nature Astronomy, 4, 1158. doi:10.1038/s41550-020-1150-z
Podio, L., Codella, C., Lefloch, B., et al. 2017, MNRAS, 470, L16. doi:10.1093/mnrasl/slx068
Pokhrel, R., Myers, P. C., Dunham, M. M., et al. 2018, ApJ, 853, 5. doi:10.3847/1538-4357/aaa240
Rodríguez-Fernández, N. J., Tafalla, M., Gueth, F., et al. 2010, A&A, 516, A98. doi:10.1051/0004-6361/201013997
Rouaud, M., Wakelam, V., & Hersant, F. 2016, MNRAS, 459, 3756. doi:10.1093/mnras/stw887
Schwörer, A., Sánchez-Monge, Á., Schilke, P., et al. 2019, A&A, 628, A6. doi:10.1051/0004-6361/201935200
Seifried, D., Banerjee, R., Pudritz, R. E., et al. 2015, MNRAS, 446, 2776. doi:10.1093/mnras/stu2282
Stephens, I. W., Bourke, T. L., Dunham, M. M., et al. 2019, ApJS, 245, 21. doi:10.3847/1538-4365/ab5181
Suzuki, H., Yamamoto, S., Ohishi, M., et al. 1992, ApJ, 392, 551. doi:10.1086/171456
Takakuwa, S., Saigo, K., Matsumoto, T., et al. 2017, ApJ, 837, 86. doi:10.3847/1538-4357/aa6116
Taniguchi, K., Herbst, E., Ozeki, H., et al. 2019, ApJ, 884, 167. doi:10.3847/1538-4357/ab3eb8
Taniguchi, K., Ozeki, H., Saito, M., et al. 2016, ApJ, 817, 147. doi:10.3847/0004-637X/817/2/147
Taniguchi, K., Saito, M., Hirota, T., et al. 2017, ApJ, 844, 68. doi:10.3847/1538-4357/aa7899

- Valdivia-Mena, M. T., Pineda, J. E., Segura-Cox, D. M., et al. 2022, A&A, 667, A12.
doi:10.1051/0004-6361/202243310
- van der Tak, F. F. S., Black, J. H., Schöier, F. L., et al. 2007, A&A, 468, 627. doi:10.1051/0004-6361:20066820
- Vastel, C., Bottinelli, S., Caux, E., et al. 2015, SF2A-2015: Proceedings of the Annual meeting of the French Society of Astronomy and Astrophysics, 313
- Vorobyov, E. I., Steinrueck, M. E., Elbakyan, V., et al. 2017, A&A, 608, A107. doi:10.1051/0004-6361/201731565
- Yang, Y.-L., Sakai, N., Zhang, Y., et al. 2021, ApJ, 910, 20. doi:10.3847/1538-4357/abdfd6
- Zucker, C., Schlafly, E. F., Speagle, J. S., et al. 2018, ApJ, 869, 83. doi:10.3847/1538-4357/aae97c